Interfacial engineering of conformal titanium oxide nanofilms on porous carbon supercapacitor electrodes via atomic layer deposition

Remuel Isaac M. Vitto [a,*], Hamed Pourkheirollah [a], Jari Keskinen [a], Steffen Vindt [b], Andrew Cook [c], Līga Grīnberga [d], Līga Ignatāne [d], Gints Kučinskis [d], Amit Tewari [a], Donald Lupo [a], Paul R. Berger [a,e], Matti Mäntysalo [a]

[a] *Faculty of Information Technology and Communication Sciences, Tampere University, Finland*
[b] *InnoCell ApS, Svendborg, Denmark*
[c] *Beneq Oy, Espoo, Finland*
[d] *Institute of Solid State Physics, University of Latvia, Latvia*
[e] *Department of Electrical and Computer Engineering, Ohio State University, USA*
**Corresponding author. Email: remuel.vitto@tuni.fi*

Keywords

Atomic layer deposition, Titanium dioxide, Growth per cycle, Activated carbon, Supercapacitors, Printed electronics, Specific capacitance, Equivalent series resistance

Abstract

Atomic layer deposition (ALD) has been gaining in popularity as a powerful deposition technique and have been shown to be a promising interfacial engineering method to boost the electrochemical performance of supercapacitors, bridging the gap in energy density. In that regard, we developed an ALD technique to deposit titanium dioxide (TiO_2) nanofilms onto porous activated carbon (AC) electrodes. This study focused on the critical aspects of the ALD process that were still unexplored by previous relevant works, including the effects of precursor pulse duration and film thickness on the complex porous structures of AC. In particular, these comprehensive investigations pave the way towards uniform distribution and excellent conformity of the TiO_2 nanofilms across the AC surface. Moreover, the deposited films were found to be amorphous and resulted in increased amounts of oxygen-containing surface functional groups. The enhanced electrochemical behavior from the TiO_2 nanofilms were found to be optimal at 60 ALD cycles with an estimated film thickness of 2.3 nm. The assembled supercapacitor device coated with this ALD technique exhibited higher specific capacitance compared to the bare AC. The key findings of this work provide the foundation of an effective strategy using ALD for fabricating new electrode materials for high-performance supercapacitors.

I. Introduction

Supercapacitor (SC) devices are a promising energy storage solution to the ever more demanding modern technological world that equally demands more powerful energy sources. However, there are currently limited opportunities for SC technology in industrial applications since they still suffer from relatively low energy density when compared to commercially available lithium-ion batteries (LiBs). The most typical market-ready SCs based on carbonaceous materials, especially activated carbon (AC), only have an energy density of around 2.3 to 8 Wh kg^{-1} [1], while the typical commercial LiBs boast relatively high energy density of up to 280 Wh kg^{-1} [2,3]. Despite this disadvantage, SCs have advantages over batteries such as their ability to deliver their energy at a superior power output. Producing SCs with energy densities comparable to LiBs will overcome their limitations, unlocking a promising new solution for the energy demands of the modern world.

It is important throughout this quest for superior energy dense SCs to employ non-toxic materials and maintain their eco-friendliness and non-carcinogenic, mutagenic, and or toxic for reproduction (CMR) qualities. This consideration makes ACs derived from waste biomass materials a highly appealing baseline candidate electrode. The energy storage mechanisms for AC-based SCs are primarily through the formation of electric-double layer capacitance (EDLC) between the electrode surface and the electrolyte ions. A common strategy to enhance the energy density of AC SCs is to increase the overall capacitance by combining the EDLC with surface chemistry of nanostructures such as Transitional Metal Oxides (TMOs) that undergo faradaic redox reactions known as pseudocapacitance (PC) [4,5,6]. However, it is crucial that the TMO nanostructure decorations retain the unique and intricate porous structures of the substrates. This characteristic property of ACs is responsible for their extremely high surface area that allows more active sites in the formation of electric-double layers for higher capacitance. Several physical and chemical coating techniques of TMOs onto ACs and other carbon-based electrodes were developed over the years including hydrothermal [7], precipitation [8], calcination [9], electrodeposition [10], sol-gel [11], and chemical vapor deposition [12]. However, these material engineering techniques face several challenges regarding the preservation of porous structures including relatively large granules and agglomeration, reduced surface area due to the pore blockage, uncontrolled growth thickness, and lack of coating uniformity.

In recent years, a coating technology known as atomic layer deposition (ALD) has attracted the attention of researchers for its powerful ability to deposit films with excellent uniformity and conformality in the nanoscale. Furthermore, ALD involves cost-effective processes that parallel the sustainability objectives of ACs thanks to its precise atomic layer-by-layer growth of nanostructured films that significantly reduces the waste from excess elements [13]. The ALD technique has come a long way since its invention by Suntola and Antson in mid 1970s [14] and it is now making its way into the realm of electrochemical energy storage devices: LiBs, sodium-ion batteries (NiBs), and SCs [15,16, 17]. Among the selection of various TMOs, titanium dioxide (TiO_2) is one of the most sought-after materials in electrochemical applications for its low-cost and excellent chemical stability [18]. In addition, electroactive materials such as TiO_2 possess remarkable advantages in their electrochemical properties as they reach the scale of nanoparticles. However, the carcinogenicity and mutagen toxicity of TiO_2 remains unclear [19,20]. Hence, further evaluations are required to clarify its potential hazards.

Wang *et al*. [21] fabricated electrodes based on TiO_2 nanofilms (7-30 nm) on glassy carbon substrates and determined their pseudocapacitive behavior as a factor of particle size. The voltammetric measurements showed increasing amounts of overall stored charge and significantly faster charge/discharge cycles as the particle sizes decrease below 10 nm. These findings further reinforce the benefits of utilizing the ALD technique to deposit TiO_2 nanofilms on AC electrodes to enhance its overall SC performance. Moreover, the three-dimensional (3D) interconnected porous structures and high surface area of ACs offer an effective solution to fabricate small enough TiO_2 nanoparticles. To counter the hindered capacitive abilities of bulk TiO_2 particles due to slow molecular transport of ions in the network, Brezesinski *et al*. [22] studied templated nanocrystal-based porous TiO_2 films and observed that both the mesoporous morphology and nanocrystals templates to be key in having high levels of capacitive charge storage due to shorter diffusion path lengths for ion transport. Previous studies on the ALD coating of TiO_2 films on ACs include the works of Tan *et al*. [23] and Bai *et al*. [24] where they have observed increased overall capacitance and energy density values at a wider potential window and higher retention. However, both these studies have only confirmed the presence

of the TiO_2 in their AC electrodes through elemental mapping analysis but failed to employ more conclusive characterizations on the overall quality of the ALD-deposited coatings. Especially that their elemental mapping studies were performed at low magnifications which fails to provide if the coatings are individualized bulk particles or uniformly coated layers. In this regard, developing a technique that produces TiO_2 nanofilms with excellent uniformity and conformity on such complex 3D surfaces of AC still remains to be a challenge.

In this study, we report a comprehensive approach in establishing an ALD technique to deposit uniform and conformal nanofilms of TiO_2 onto porous AC electrodes for SC devices. Herein, we explore the importance of precursor pulse times to promote excellent surface coverage and higher growth rate values for a more efficient but effective technique. In contrast to previous work, which relied on high deposition temperature of 180-300°C [25,26,27], we have developed an ALD process at a low temperature of 120°C that ensures it can be utilized in a wide range of substrates and binders. This is a critical aspect when considering the applicability of ALD in SCs which are typically composed of thermally sensitive materials. Moreover, the possibility of pore blocking and optimal TiO_2 film thickness is studied through performing varying number of ALD cycles. The TiO_2-coated AC electrodes were assembled into symmetrical SCs to determine the positive effects of the TiO_2 nanofilms in terms of increase in capacitance and higher operating voltage. Overall, this study provides a thorough investigation on the effects of ALD parameters and proposes a powerful technique to deposit TiO_2 nanofilms on AC SC electrodes for improved electrochemical performance.

II. Experimental section

3.1. Electrode fabrication

The AC ink is composed of 90 wt% YP-80F as the electrode material and 10 wt% SBR-CMC mixture as the binder. Prior to ink preparation, a diluted solution at 2 wt% CMC and 40 wt% SBR with DI water was mixed. To prepare the AC ink, 28 g of the CMC solution and 0.12 g of laboratory grade Triton X-100 (Sigma-Aldrich) were slowly added to 14 g of YP-80F. Approximately 30 g of DI water was added to the mixture and stirred continuously using an Ultra-Turrax T 10 basic homogenizer. Lastly, 3.2 g of the SBR solution was added under stirring and small amounts of DI water was slowly added until the desired viscosity of the ink was reached. The prepared ink was then transferred to a syringe and kept in a desiccator until further use.

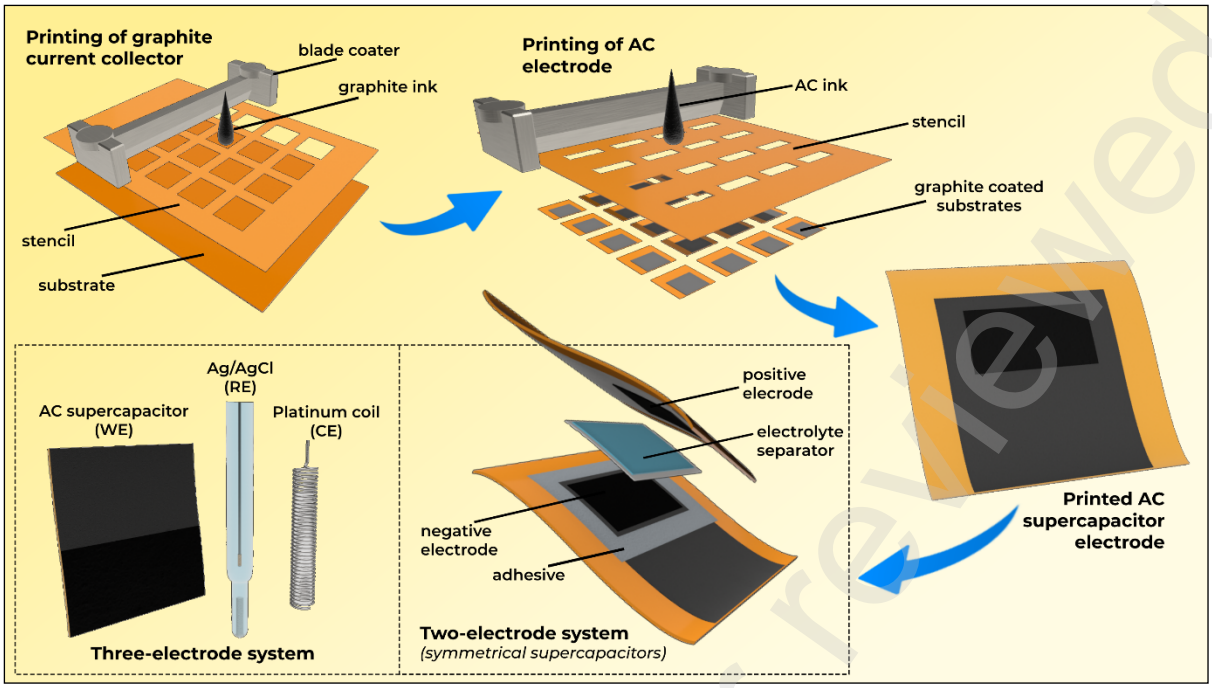

Figure 1. Schematic illustration showing the fabrication process of the graphite current collector and AC electrodes on PI substrates using doctor blade coater. The fabricated electrodes with/without ALD coatings are then utilized in a two-electrode system as symmetrical SC devices, and in a three-electrode system with Ag/AgCl reference electrode and platinum counter electrode.

The SCs consist of the YP-80F main electrode and the EDAG graphite current collector on 100 µm Kapton PI film substrates. Fig. 1 shows a schematic illustration of the whole SC electrode fabrication. While a 50 µm wide Kapton PI film was utilized as the stencil and the electrode patterns were cut through a Silhouette Cameo 3 machine. The PI film substrate was placed underneath the stencil and a generous amount of graphite ink was spread onto the side of each cutout. Afterwards, a 220 mm mtv-messtechnik doctor blade coater was used to print the graphite current collectors and dried in an oven for an hour at 95°C. Likewise, the YP-80F electrode was printed in the same manner atop the graphite layer but the prepared AC ink was used instead and was left to dry at room temperature overnight. Once dried, a Mitutoyo 543-250b digital indicator was used to measure the layer thickness of the graphite current collector and AC electrode of around 25-35 µm and 30-40 µm, respectively.

3.2. Atomic layer deposition

The TiO_2 nanofilms were grown using a Beneq TFS 200 ALD system directly on the fabricated SC electrodes and 50 mm diameter silicon wafers (Siegert Wafer) as dummy samples for thickness measurement. A schematic illustration for a single ALD cycle is shown in Fig. 2. Titanium tetrachloride ($TiCl_4$) from Volatec Ltd. was utilized as the titanium source and deionized water was utilized as the oxygen source. The chemical reactions involved in the growth mechanism of TiO_2 films are as follows [28]:

(A) $$TiOH\,(s) \;+\; TiCl_4\,(g) \;\rightarrow\; TiO-TiCl_3\;(s) \;+\; HCl\,(g) \qquad (1)$$

(B) $$TiCl\,(s) \;+\; H_2O\,(g) \;\rightarrow\; Ti-OH\,(s) \;+\; HCl\,(g) \qquad (2)$$

The sequential completion of reactions A and B constitutes one ALD cycle of TiO_2 deposition and initiated at the hydroxyl (OH) covered surface of either the AC electrode or previously

deposited oxygen layer. The ALD reaction sequence involves the four-step process: (i) the OH groups react with the $TiCl_4$ precursor; (ii) nitrogen purging of excess $TiCl_4$ precursor and hydrochloric acid (HCl) by-products; (iii) the TiCl species from the titanium layer react with the H_2O precursor; (iv) nitrogen purging of excess H_2O precursor and HCl by-products.

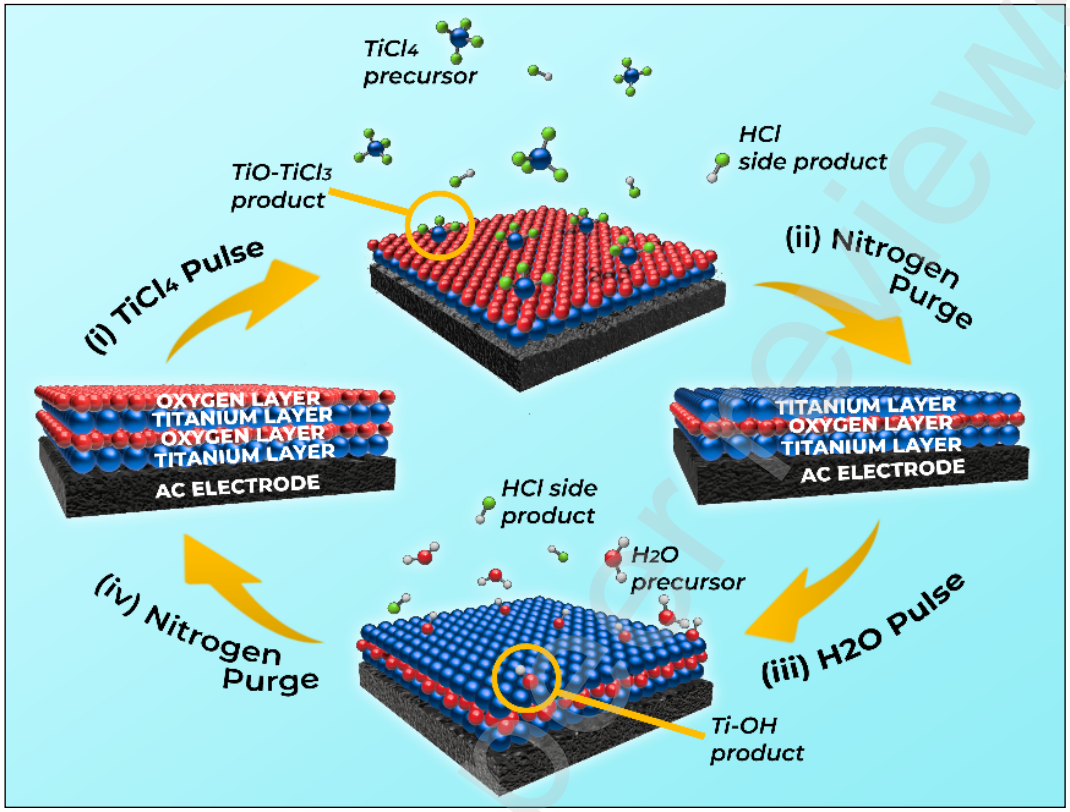

Figure 2. Schematic illustration of the ALD of TiO_2 on AC electrodes involving a $TiCl_4$ precursor and H_2O precursor pulses followed by a nitrogen purge. This four-step process constitutes one ALD cycle which is repeated over several times until the desired nanometer thickness is achieved [28].

These chemical reactions provide the practical requirements of precursor pulse duration. The ideal ALD growth mechanism should involve full surface saturation of the TiO-$TiCl_3$ and Ti-OH species during steps (ii) and (iv). Having insufficient precursor pulse limits the formation of these essential chemical compounds and results in a non-uniform growth of TiO_2 films. Thus, the pulse times of both precursors were incrementally increased until full saturation of the growth rate was achieved. The ALD technique was carried out at a deposition temperature of 120 °C and both nitrogen purges were kept at 5 s, while the $TiCl_4$ pulse time was varied at 50 ms, 100 ms, 150 ms, 200 ms, 250 ms, 300 ms, and 450 ms at different H_2O pulse times of 150 ms, 300 ms, and 450 ms. Once the optimal pulsing duration for both precursors was determined, the number of ALD cycles was varied to study the most effective film thickness. The TiO_2 ALD-coated electrodes used in this study and the corresponding film thicknesses measured on co-loaded silicon substrates are summarized in Table 1.

Table 1. Summary of the ALD-coated AC electrodes used in this study

	TiAC20	TiAC40	TiAC60	TiAC80	TiAC100
No. of ALD cycles	20	40	60	80	100
TiO_2 film thickness	1.6 nm	1.8 nm	2.3 nm	3.0 nm	4.0 nm

3.3. Material characterization

The growth behavior of the TiO_2 nanofilms were examined using a Rudolph Research AutoEL ellipsometer to measure the film thickness on co-loaded silicon substrates. X-ray diffraction (XRD) analysis was performed using Malvern Panalytical Empyrean machine to study the crystal structure of the fabricated AC SC electrodes and the deposited TiO_2 coating. The orientation and surface defects of bare and TiO_2 ALD-coated AC electrodes were characterized by Raman spectra measured via a Renishaw inVia Qontor integrated with 50× objective confocal microscope. A diode-pumped solid-state laser (532 nm) was used with a power of 30 mW. The spectrum was recorded as an average of 10 acquisitions of 40 s from 100 to 3200 cm^{-1}. X-ray photoelectron spectroscopy (XPS) analysis was utilized to identify surface functional groups using an Omicron Nanotechnology GmbH ESCA Model 3000 instrument under ultra-high vacuum (UHV) conditions, maintaining a base pressure below 1×10^{-10} mbar. Monochromatized Al Kα radiation (hν = 1486.5 eV) served as the excitation source. Data acquisition and analysis were carried out using CasaXPS software (version 2.3.22 PR1.0). Spectral fitting involved Shirley background subtraction followed by peak deconvolution using a symmetrical Gaussian-Lorentzian function, with a 50% Gaussian and 50% Lorentzian character for all component peaks. The surface morphology of AC electrodes before and after TiO_2 ALD decoration was characterized using a high-resolution TESCAN CLARA field emission scanning electron microscope (FESEM). The elemental composition of the TiO_2-coated AC electrodes was studied using a Zeiss Ultraplus SEM equipped with Oxford Instruments X-MaxN energy-dispersive x-ray spectroscopy (EDX). The uniformity and conformality of the TiO_2 nanofilms were closely studied on the cross-sectional portion of the AC electrodes. The lamellae were prepared using a focused ion beam scanning electron microscope (FIB-SEM) Helios 5 UX DualBeam. The surface of the lamella was protected by depositing carbon with an electron beam (e-dep. C), and a thicker platinum layer was deposited with an ion beam (i-dep.Pt) afterwards. The surface was not exposed to electrons or ions before the protective layer was created. The final thickness of lamellae was below 100 nm. The cross-sections of AC electrodes were investigated with tunneling electron microscope (TEM) Fei Tecnai G2 F20 equipped with EDX detector.

3.4. Electrochemical measurements

The fabricated AC electrodes with, and without, TiO_2 nanofilms were assembled into symmetrical SCs as shown in the schematic illustration in Fig. 1. A pre-cut 3M 468MP adhesive transfer tape was applied to the graphite and PI substrate surface leaving the AC layer exposed. Then a 40 μm Dynacap GT 0.45/40 cellulose paper soaked in a 5:1 mass ratio of water and sodium chloride (NaCl, 99.5% Sigma-Aldrich) was placed in the exposed area of the electrode with adhesive. Finally, a second AC electrode was pressed and sealed firmly to the prepared electrode with their patterns in symmetry but opposite directions. The assembled SC devices were first assessed in a two-electrode system to define their specific capacitance (C_s) and equivalent series resistance (ESR) values using a Maccor 4300 workstation. These performance metrics were calculated from an extensive charge-discharge cycle measurements based on the guidelines provided by the international industrial standard IEC 62,391-1 [29]. This measurement includes four cycles of charging and discharging using an applied current of 1, 3, and 10 mA within the values of the set operating voltage range where the fourth cycle is held constant at the upper voltage limit for 30 minutes. The upper voltage limit was set to a value of 1.0, 1.2, or 1.4 V to examine the behavior of the TiO_2 nanofilms at different voltages. The Cs and ESR values were calculated based on the following mathematical formulas:

$$C_s = 4 \times \frac{I\,\Delta t}{m\,\Delta V} \quad (4)$$

$$ESR = \frac{V_{drop}}{\Delta I} \quad (5)$$

where I is the applied current; Δt is 80% to 40% of the discharge time for the fourth cycle at 1 mA; m is the combined mass of the two AC electrodes; V_{drop} is the voltage at the IR drop of the fourth cycle at 10 mA; and ΔI is the change in current during the V_{drop}. Once the optimal thickness of the TiO_2 nanofilms was determined based on its C_s and ESR, the electrochemical behavior of the fabricated electrode with corresponding ALD cycles have been further studied as the working electrode in a three-electrode system utilizing a silver/silver-chloride (Ag/AgCl, redoxme AB) reference electrode, platinum coil counter electrode (redoxme AB), and the same NaCl electrolyte solution. Zahner Zennium potentiostat was used to perform cyclic voltammetry (CV) analysis within the potential window of 0 to 0.8 V vs Ag/AgCl and the upper potential limit is increased to 1.0 V, 1.2 V, and 1.4 V at a scan rate of 10 mV/s. The electrode-electrolyte stability behavior was also studied in the potential window of 0 to 1.2 V vs Ag/AgCl by varying the scan rate from 10 mV/s up to 100 mV/s.

III. Results and Discussion

4.1. Initial challenges and strategies of ALD

Our early attempts to deposit nano thin films of TiO_2 were done with plasma-enhanced ALD (PE-ALD) processes, a coating technique that offers several advantages such as faster nucleation of precursors and higher growth rate. The thermal energy required to activate the surface for deposition is greatly reduced due to the highly reactive plasma species [30]. The PE-ALD technique was performed on AC electrodes based on our previous works [31] made from a mixture of commercial Kuraray YP-80F powder and chitosan binder (Sigma-Aldrich, 50494) with graphite (Acheson EDAG PF-407C) current collectors and aluminum/ polyethylene terephthalate (Al/PET) substrates as shown in Figure S1. The growth rate was calculated to be 1 Å/cycle and the number of ALD cycles varied between 20 and 100 resulting to film thicknesses of 2 nm and 30 nm, measured on co-loaded silicon substrates via ellipsometry. In contrast, the surface of the coated electrodes appears to have a strong discoloration of a dark metallic blue which obviously indicates that the TiO_2 coatings are thicker than 2 nm. This signifies an uncontrolled and non-saturating growth mechanism similar to chemical vapor deposition. More importantly, the coated electrodes disintegrate when it comes into contact with a liquid solution as shown in Figure S2. This occurs when the binder of the AC electrode suffers extreme decomposition from the bombardment of the energy from the highly reactive plasma, causing the YP-80F powder to become loose and separate easily from the graphite current collector. Thus, the PE-ALD technique was deemed unfit for the application of this study, and thermal ALD was subsequently investigated.

Besides the ALD processes itself, the various material components of the AC electrodes must be taken into serious consideration for compatibility. Because the traditional thermal ALD technique used in this study is performed with a deposition temperature of 120°C and the PET component of the substrates have a glass transition temperature within the range of 50°C to 90°C [32], a more thermally stable substrate should be utilized instead. Thus, Kapton polyimide films (PI, DuPont de Nemours, Inc.) were used as substrates in this study. Their favorable properties include high thermal stability which fits very well for ALD depositions, good electrical insulation ideal for electrode substrates, and excellent mechanical flexibility that is advantageous in wearable and portable device applications of SCs [33]. Following these, TiO_2 nanofilms were successfully deposited onto the AC-chitosan electrode with PI substrates at

various number of cycles and subsequently assembled into symmetrical SCs for electrochemical characterizations as shown in Figure S3. However, the specific capacitance (Cs) and equivalent series resistance (ESR) values reveal negligible differences with the pristine sample and declines beyond 100 ALD cycles. Upon closer inspection of the coated electrodes, the chitosan binder undergoes degradation similar to the PE-ALD, however, it is thermally induced and only becomes apparent after prolonged exposure to high temperature, such as during a high number of ALD cycles. Figure S4 shows the exfoliation of the AC electrodes into bulk powders upon exposure to deionized (DI) water. For this reason, the AC-chitosan electrodes are incompatible for ALD applications and a mixture of styrene-butadiene rubber latex (SBR, MTI Corporation) and sodium carboxymethyl cellulose (CMC, Sigma-Aldrich) binder was substituted in subsequent experiments for its appealing properties. The CMC matrix acts as the main binder while the SBR improves mechanical flexibility and electrode adhesion [34]. This binder combination has an impressive thermal stability at a relatively high temperature of 288°C with a negligible small weight percentage loss of 0.8% [35].

4.2. Material Characterizations

To critically assess the amount of TiO_2 deposited onto the AC surface per ALD cycle, the measured thickness is normalized by the number of cycles used and defined as the growth rate or growth per cycle (GPC). Fig. 3a shows the computed GPC values of the TiO_2 layer versus the $TiCl_4$ pulsing duration at three different values of H_2O pulse time using a fixed number of 100 ALD cycles. The growth rate is observed to increase at a faster rate when the $TiCl_4$ pulse time is increased within the range of 50 ms to 150 ms. However, the growth rate began to saturate when the precursor pulse time reached 200 ms and eventually plateaued beyond 300 ms at 0.6 Å/cycle. This growth behavior signifies the saturation point in the ALD process which occurs at the "self-limiting region" where no further chemical reaction from the precursors occurs. Interestingly, higher GPC values and increased uniformity of refractive index are observed as the H_2O pulse times are increased. For this reason, the pulsing duration for H_2O was determined to be optimal at 450 ms and was kept constant in the succeeding ALD processes. Concerning the growth mechanism on the silicon substrates, there is not any significant difference from increasing the $TiCl_4$ pulse time further than 200 ms as they all saturate at 0.6 Å/cycle. Nevertheless, it becomes a critical aspect, and the difference is magnified during the actual depositions when the AC electrodes are present in the ALD chamber. To investigate this further, the growth rate of the actual depositions at varying number of ALD cycles were done at 200 ms and 450 ms of $TiCl_4$ pulse time as shown in Fig. 3b. Increasing the $TiCl_4$ pulse time results in higher GPC values which indicates a non-saturating growth behavior at 200 ms, although it is within the self-limiting region. This occurs possibly because of the marginal increase in surface area of the AC electrode substrates which requires significantly longer pulsing times when compared to silicon wafers alone. Additionally, the 200 ms pulse time is at the early stages of saturating behavior. As such, the growth rate is much more stable in the later stages of the self-limiting region and the optimal pulse time values for $TiCl_4$ precursor for AC electrode applications are determined to be 450 ms. In addition, the GPC values for the actual depositions stabilized around 0.4 Å/cycle similar to the growth rate achieved for $TiCl_4$ and H_2O precursors by Ritala et al. [28].

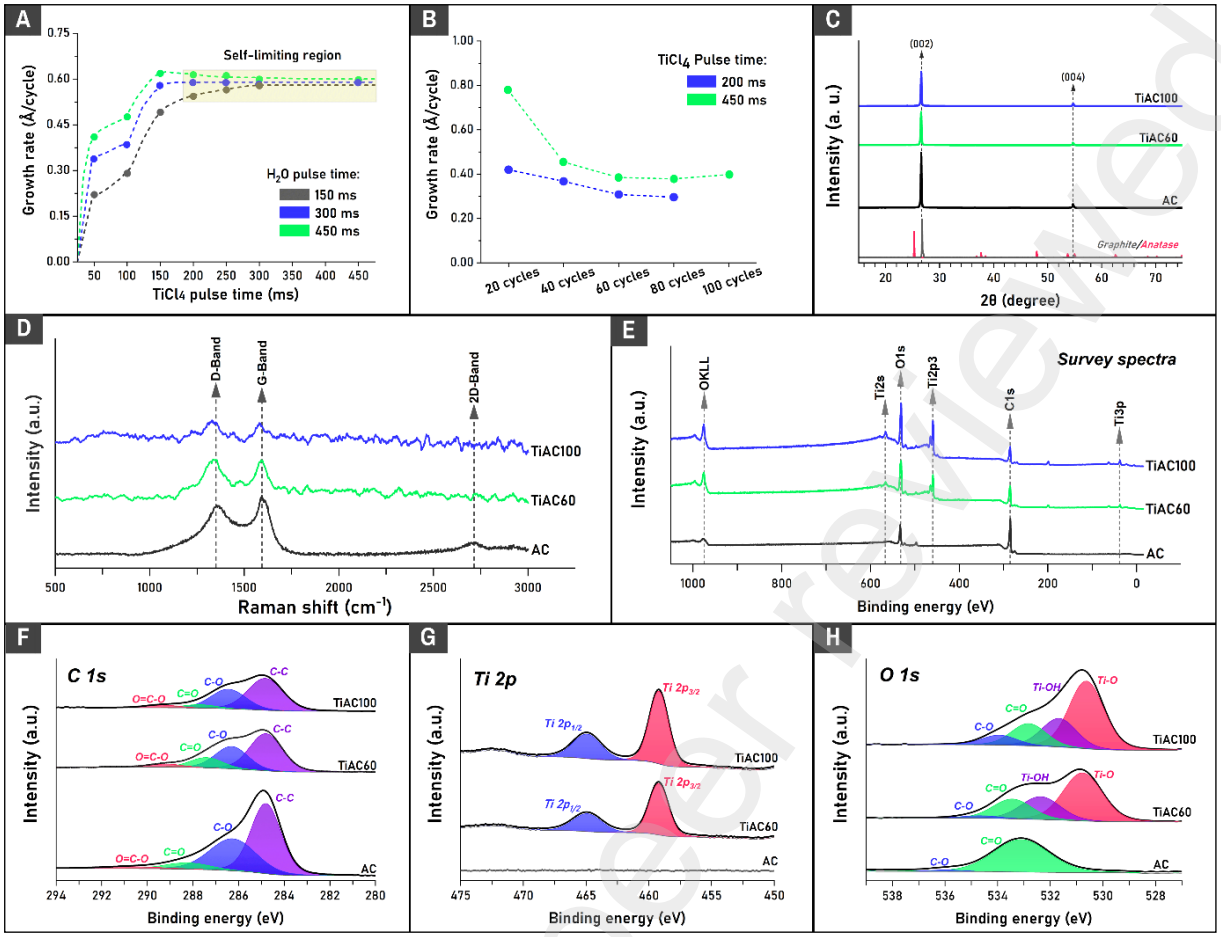

Figure 3. Material characterizations of the TiO_2 nanofilms deposited via ALD. Growth per cycle behavior (a) as a function of $TiCl_4$ pulse time at different H_2O pulse times and (b) as a function of ALD cycle amount at 200 ms and 450 ms pulse time of titanium tetrachloride. (c) XRD graphs of bare and coated AC electrodes, insets are the reference peaks for graphite and anatase structure. (d) Raman spectroscopy of bare and coated AC electrodes. (e) XPS survey spectra of bare and coated AC electrodes. Deconvoluted and fitted peaks for the regions: (f) C 1s, (g) Ti 2p, and (h) O 1s.

Following the analysis of TiO_2 growth mechanisms, the deposited films with varying thickness underwent comprehensive materials characterizations based on their crystallinity, structural defects, surface functional groups, surface morphology, and elemental composition. Fig. 3c shows the XRD spectra of bare AC and coated electrodes TiAC60 and TiAC100. To further analyze the corresponding peaks, reference peaks from the graphite (RRUFFID No. R050503) and anatase (RRUFFID No. R070582) crystal structures are shown as an inset at the bottom of the figure. All the samples exhibited a strong peak at 26.5° and a slight peak at 54.5°, consistent with the peaks present in the reference crystalline graphite. These two peaks correspond specifically to the (002) and (004) planes of the graphite crystal structure. Moreover, it can be observed that the crystalline graphite peaks reduce in intensity as the ALD cycles increase. This can be attributed to the increasing film thickness which decreases the penetration depth of the x-rays and reduces the signal coming from the AC layer. A few nm thin and most likely amorphous TiO_2 films are present on the surface, thus peaks corresponding to TiO_2 cannot be observed in the XRD data.

Fig. 3d shows the Raman spectra of the bare and TiO_2-coated AC electrodes where the presence of prominent D and G bands, and a weak 2D band signature are confirmed in the bare AC sample. However, in the case of the TiAC60 and TiAC100, the intensity of the prominent

peaks seemingly diminishes and is unable to present any impression of the 2D band. This occurs due to the similar interactions which were observed in the XRD measurements where the signal generated from the AC layer decreases as the number of ALD cycles increases. Generally, the D band represents the inelastic scattering of the phonon from the defect sites and the G band infers the presence of ordered graphitic structure due to vibrational stretching of sp^2 hybridized carbon. Whereas the 2D band arises from a second-order overtone, as a result of the interactions between the incident laser and charge carriers causing two sequential inelastic scattering events from two distinct phonons instead of scattering from defects [36]. Aside from these characteristic peaks, a high intensity ratio between the D and G bands (I_D/I_G) also provides information about the number of defects present in the surface. The I_D/I_G ratio was calculated to be 0.87 for AC, 1.01 for TiAC60 and 1.02 for TiAC100. The persistent structural disorder observed in AC is attributed to a high density of defect sites located at the edges of its flakes [37]. Although the AC samples coated with TiO_2 nanofilms have higher I_D/I_G ratio than the pristine sample, which infers higher surface defect sites, taking into consideration that these are muted peaks from the AC layer rather than the TiO_2 layer. Note that amorphous TiO_2 does not produce Raman peaks [38]. As such, the XRD and Raman studies provide inconclusive characterizations regarding the uniformity and overall quality of the TiO_2 nanofilms. Moreover, the surface morphology studies discussed later in this section provide a sounder explanation which has probably caused higher surface defects in the ALD-coated samples.

The XPS survey scan of the bare and TiO_2-coated AC electrodes presents all the constituent elements present on the surface as shown in Fig. 3e. From there, the peaks corresponding to titanium and oxygen such as O KLL, Ti 2s, O 1s, Ti 2p, and Ti 3p are already apparent and increase in intensity as the number of ALD cycles gets higher. While the C 1s peak decreases as the TiO_2 layer thickness increases, which is consistent with the XRD and Raman analysis. Each of the several significant peaks are then deconvoluted to provide a more in-depth analysis and reveal their specific functional groups. Fig. 3f shows the C1s spectrum which are mainly separated into four following components: sp^2 hybridized (C-C, 284.8 eV), hydroxyl (C-O, 285.9 eV), carbonyl (C=O, 286.8 eV), and carboxyl (O=C-O, 289.5 eV) [39,40,41]. While the doublet peaks Ti $2p_{1/2}$ (464.9 eV) and Ti $2p_{3/2}$ (459.2 eV) associated to the Ti 2p are shown in Fig. 3g. The peak separation of 5.7 eV between the two Ti 2p peaks is in excellent agreement with the reported values in previous relevant studies [25,26]. As expected, both of the Ti 2p peaks are exclusive to the TiO_2-coated AC samples where the TiAC100 sample displayed the highest intensity. Lastly, the deconvoluted peaks associated with O 1s shown in Fig. 3h are primarily composed of only the hydroxyl (C-O, 536 eV) and carbonyl (C=O, 533.1 eV) groups for the pristine AC samples [42]. Upon which, the TiO_2 coating led to two additional peaks of hydroxyl (Ti-OH) groups located at 532.4 eV and 531.7, and titanium oxide (Ti-O) groups located at 530.8 eV and 530.7 for TiAC60 and TiAC100, respectively. The Ti-OH peak is primarily due to the non-lattice adventitious oxygen atoms at the surface brought by the ALD deposition while the Ti-O peak corresponds directly to the crystal lattice of the deposited TiO_2 layer, specifically from the coordination of O^{2-}-Ti^{4+} atoms to form the TiO_6 octahedron [43]. Thus, the XPS measurements undoubtedly confirm the presence of ALD-coated TiO_2 layers at the surface of the AC electrodes but further material characterizations such as SEM, EDX, and TEM are required to confirm their uniformity and conformity.

The surface morphology of the AC electrodes was characterized through high-magnification SEM images to analyze pore blocking behavior and quality of surface coverage of the TiO_2 nanofilms as shown in Fig. 4a to f. The typical layered graphitic structure of bulk AC particles is observed across all samples similar to the YP-80F morphology reported by Fic et al. [44] at

comparable magnifications. Although, interesting nanostructures were spotted on selected areas of the surface of TiO_2-coated AC electrodes. Higher magnification SEM images (Fig. 4e and f) showed cubic-shaped crystal nanostructures with varying particle diameters of around 100 nm to 400 nm. The TiAC100 sample was further studied using EDX and elemental mapping analysis was performed on a site containing that nanostructure to study its composition as shown in Fig. 4g and S5a. The distribution of the elements on the surface of the TiAC100 sample reveals a density of sodium (Na) and chlorine (Cl) elements localized on the area of the cubic nano structures shown in Fig. S5b and c, respectively. The elemental composition and cubic morphology of the nanostructures found on the TiO_2-coated AC electrodes are consistent with NaCl nanocrystals synthesized by Wang et al. [45]. The formation of these compounds most likely occurred during the ALD process as a side reaction between the sodium atoms from the CMC binder and the highly reactive $TiCl_4$ precursors or HCl by-products. Also, these NaCl nanocrystals could be considered as defect sites on the surface of the electrodes from a surface point of view and may have been the cause for higher I_D/I_G ratio for the TiO_2-coated ACs. Nevertheless, Fig. 4h to j shows the elements of interest such as C, Ti, and O to have a uniform distribution across the surface of TiAC100 sample. Most notably, the distribution of Ti and O elements were found to be reduced at the area of the nanostructures. As no other visible structures on the surface of TiO_2-coated AC electrodes were observed at high magnification SEM images and the surrounding graphitic structures remained consistent across all samples, the elemental mapping suggests the deposited TiO_2 layer are nanofilms with excellent uniformity and coverage.

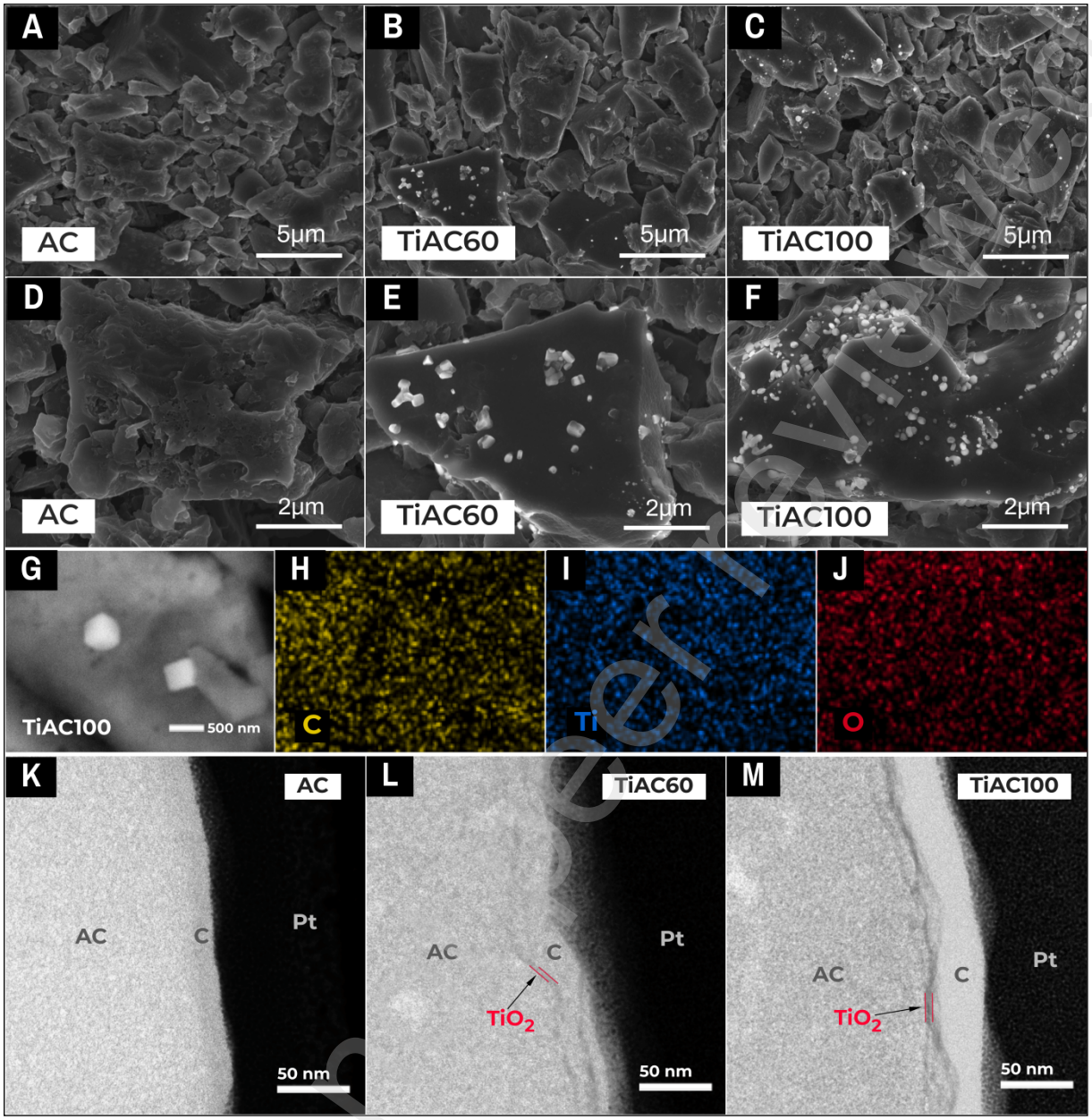

Figure 4. FESEM images at low and high magnifications of AC electrodes: (a,d) pristine, (b,e) TiAC60, and (c,f) TiAC100. (g) FESEM image of TiAC100 site selected for EDX mapping analysis of (h) C, (i) Ti, and (j) O. TEM images of AC electrodes: (k) pristine, (l) TiAC60, and (m) TiAC100.

Thus, TEM images of the AC, TiAC60, and TiAC100 were utilized to determine the uniformity and conformity of the TiO_2 layers on the AC electrode surface. As anticipated, the cross-sectional area of the pristine AC electrode only contains the AC layer, and the electron-beam deposited protective layer made of C as shown in Fig. 4k. While on the ALD-coated samples, a very thin and uniform layer of TiO_2 which appears like a hairline crack in between the AC and C layer is shown in Fig. 4l. Going to the TiAC100 sample, Fig. 4m revealed a much thicker line of the TiO_2 layer. The thickness of these observed TiO_2 layers can be easily estimated with 50 nm scale bar to be somewhere in the range of 2 to 10 nm, which are in excellent consistency with the measured TiO_2 film thickness of 2.3 nm for TiAC60 and 4.0 nm for TiAC100 based on the computed GPC values. Furthermore, a fast survey scan using EDX analysis was performed to analyze the elemental composition of each layer. The TEM images of the cross-sectional area of TiAC60 and the different sites marked O_1 to O_4 used for the study are shown in Fig. S6a and b. In the EDX spectra presented in Fig. S6c, a primary carbon peak

associated to the AC layer remained constant in intensity across all four sites. Aside from this, a minor peak for copper is observed at all the sites as a result of background radiation from the copper omniprobe grid and copper-based spacers rings used in the experimental setup of TEM and EDX. While the Ti peaks are of negligible intensities at the sites O_3 and O_4 where the supposed AC and C layers are, they increased for the sites O_1 and O_2 where the supposed TiO2 layer is. Hence, these cross-sectional TEM images coupled with the elemental analysis of EDX confirm that the ALD-deposited TiO_2 layers are conformed excellently on the underlying AC electrode surface and are in the thickness level dictated by the optimized GPC values.

4.3. Electrochemical Characterizations

The assembled symmetric SC devices were assessed in extensive charge-discharge cycles to determine the effect of the TiO_2 nanofilms on the capacitance behavior of the AC electrodes. Fig. 5a and b shows the calculated C_s and ESR values for the bare and TiO_2-coated AC SC devices as averages of four samples with 95% confidence interval error bars. The measured C_s of the bare AC SC is 102 F/g, 106 F/g, and 113 F/g for upper voltage of limits of 1.0 V, 1.2 V, and 1.4 V, respectively. Upon surface decorations of TiO_2 nanofilms, the measured Cs values increased gradually with increasing number of ALD cycles except for sample TiAC60 and onwards where the increase plateaued. It can also be noted that the improved C_s values brought by the TiO_2 nanofilms are significantly higher when the upper potential limit was increased to 1.2 V and 1.4 V. The highest C_s was observed at TiAC100 sample to be 187 F/g which is an excellent 67% improvement compared to the 113 F/g of the pristine AC SC. Although, it does not differ much with the highest C_s value displayed by TiAC60 which is at 182 F/g and is a 61% improvement from the pristine. This indicates that the TiO_2-coated AC SC with the most enhanced capacitance behavior is already achieved at 60 ALD cycles and increasing it further yields with little to no difference in C_s values. Thus, the developed ALD technique was deemed optimal at 60 cycles with an estimated TiO_2 film thickness of 2.3 nm. While the measured ESR values showed an increasing pattern upon the introduction of TiO_2 nanofilms when the ALD process reached 80 and 100 cycles. The TiAC100 sample exhibited the highest increase in ESR with a value of 7.6 Ω and 10.4 Ω for upper voltage limits of 1.2 V and 1.4 V, respectively. The increasing ESR value on the TiO_2-coated AC SC could be linked to the added oxygen-containing functional groups within the oxygen layer of the TiO_2 nanofilm as confirmed in the O 1s region of the XPS spectra in Fig. 3h. The conductivity of the electrodes is decreased by the introduction of oxygen-containing functional groups through increased defect sites, sp3 hybridization, and ohmic impedance [46]. The surface defects serve as active sites for electrolyte decomposition and parasitic faradaic reactions at high operating voltages [47]. Consequently, higher ESR values are experienced by the SCs with thicker TiO_2 nanofilms at higher upper voltage limits as observed in Fig. 5b. Regardless, an increasing trend in C_s values are still observed as the TiO_2 nanofilms are decorated on the AC electrode surface.

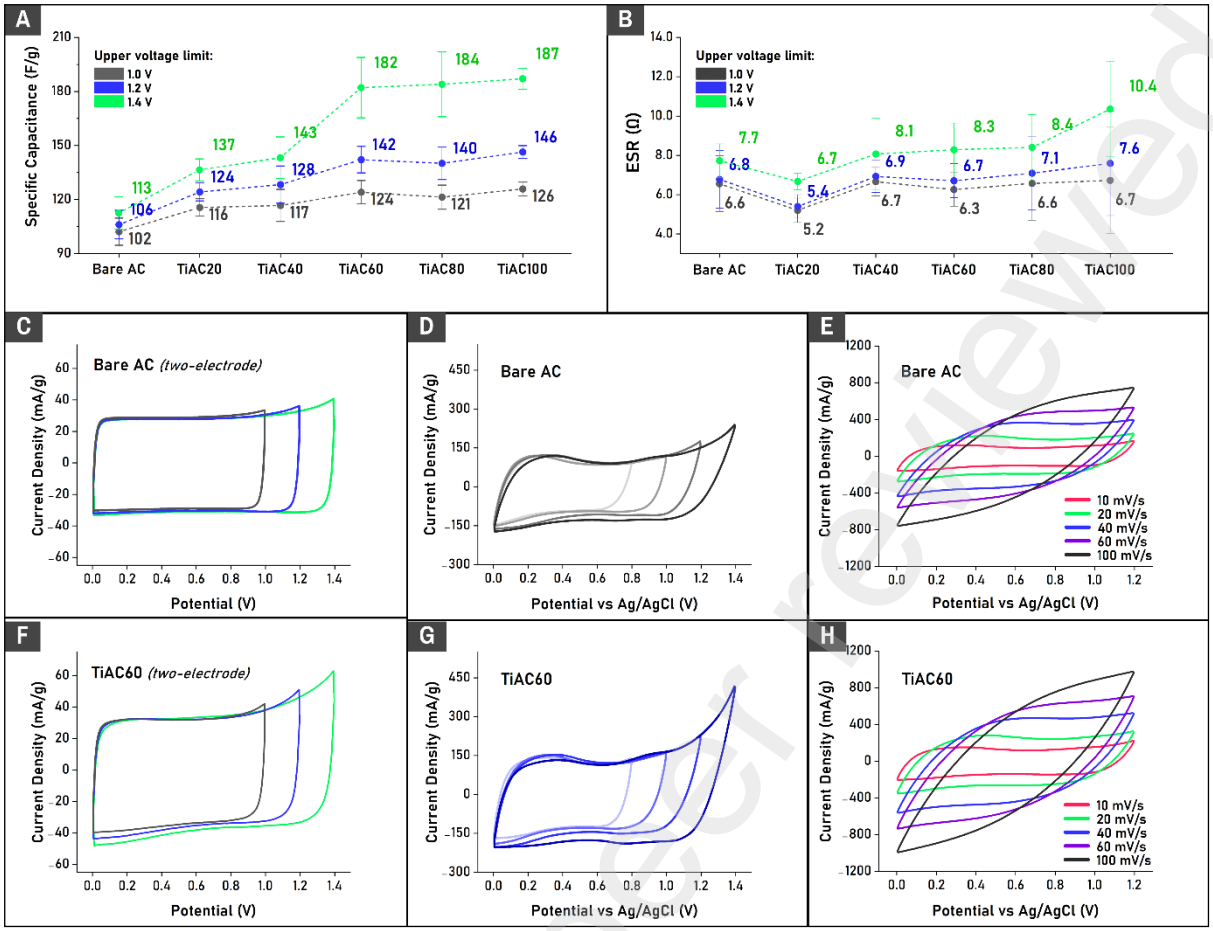

Figure 5. Calculated average values of (a) C_s and (b) ESR for the bare and TiO_2-coated AC SCs at varying upper voltage limits of 1.0 V, 1.2 V, and 1.4 V. Cyclic voltammetry curves of (c) bare and (f) TiAC60 SCs at increasing potential window at a scan rate of 10 mV/s. Three-electrode system cyclic voltammetry curves of bare AC and TiAC60 electrodes at (d,g) increasing potential window with a scan rate of 10 mV/s and at (e,h) varying scan rate within the potential window of 0.0 V to 1.2 V.

The electrochemical properties of the bare AC and TiAC60 samples were then further studied through CV to provide an in-depth qualitative analysis. Fig. 5c and f show the two-electrode system CV curves of bare AC and TiAC60, respectively. The scan rate was kept constant at 10 mV/s while the potential window of 0.0 V to 1.0 V was increased to 1.2 V and 1.4V similar to the operating voltages used for the calculation of C_s and ESR. The ideal quasi-rectangular shape of CV curves for EDLCs were observed for both SCs. However, no characteristic faradaic reduction-oxidation peaks of the TiO_2 layer were observed in the TiAC60 sample. This indicates that higher C_s values measured from TiO_2-coated AC SCs is a result of its higher electrochemical activity as observed from the larger CV curve of TiAC60 compared to the bare AC consistent with the reported results by Tan *et al.* [23] and Bai *et al.* [24]. On the CV curve of bare AC, the current reading at the right most of the oxidation curve remained stable and only increased slightly when the upper potential is increased. While on the TiAC60, evidence of the presumed electrolyte decomposition and parasitic faradaic reactions are attributed from the dramatic increase in current reading and led to the appearance of "tail"-like features at the oxidation curve when the potential window is increased.

Following this, both AC and TiAC60 samples were utilized in three-electrode system measurements of CV for a more accurate analysis of the electrochemical reactions taking place at the electrode surface. This limits the produced CV curve from a signal of only a single

electrode which would otherwise be a product of overlapping peaks from two electrodes. Fig. 5d and g show the CV curves via three-electrode measurements for bare AC and TiAC60, respectively. Considering that three-electrode systems have typically smaller potential window than two-electrode systems, the CV analysis was performed from 0.0 V to 0.8 V and increased until 1.4 V while the scan rate remains constant at 10 mV/s. In this electrochemical setup, the faradaic side reactions and the "tail"-like characteristics are more apparent especially in the TiAC60 sample. In addition, an anodic peak at around 0.90 V and a cathodic peak at 0.77 V are observed in both electrodes as the upper potential limit reached 1.2 V and 1.4 V. These peaks could be attributed to the decomposition of water molecules in the electrolyte solution as the electrochemical system reach high potentials. Although it depends on the pH level and ionic compounds present in the electrolyte solution, the electrochemical reactions which could have occurred are [48]:

at the cathode, $$2H^+\ (aq)\ 2e^- \rightarrow H_2\ (g) \quad (5)$$

at the anode, $$H_2O \rightarrow \frac{1}{2}O_2\ (g) + 2H^+\ (aq) + 2e^- \quad (6)$$

Whereas these pair of redox peaks appear more visible on the CV curve of TiAC60 compared to the bare AC probably as a result of its higher amount of oxygen-containing functional groups within the oxygen layer of the TiO_2 coating which promotes electrolyte decomposition. Consistent with the two-electrode system measurements, the TiAC60 exhibits higher capacitance values compared to the bare AC indicated by its larger CV curve area regardless of the absence of added pseudocapacitance from the TiO_2 layer. In their study, Bai *et al*. [24] claim that the ALD-deposited TiO_2 nanolayer in the SC electrodes act as dielectric capacitors and provide additional capacitance in a similar manner to parallel plate capacitors. Aside from the increased C_s values, they also claimed that the TiO_2 nanolayer establishes an inert layer which protects the electrode/electrolyte interface and increase cycling stability. As such, the bare AC and TiAC60 electrodes were investigated within the potential window of 0.0 V to 1.2 V at increasing scran rates of 10 mV/s to 100 mV/s as shown in Fig. 5e and h. Contrary to the findings of previous studies, the CV curves of bare AC and TiAC60 electrodes displayed similar transformation from a quasi-rectangular at low scan rates to an elliptical shape at high scan rates. The contrasting results could be attributed to the electrolyte solution and electrochemical setup used to characterize the electrochemical behavior. They performed the measurements in an organic electrolyte known to have a wide potential window in a more stable but less accurate two-electrode system. In this context, the observed cycling stability of the TiO_2-coated AC electrode in this study might have been limited by the smaller potential window of NaCl electrolyte and its sensitivity to the decomposition, especially when a three-electrode system was used.

IV. Summary and Conclusion

In this paper, we developed an ALD technique to coat TiO_2 nanofilms onto printed porous AC electrodes as substrates using $TiCl_4$ and H_2O precursors at a relatively low growth temperature of 120 °C. The pulse duration of both ALD precursor was investigated and prolonged times were found to be critical for the high surface area AC substrates. The self-limiting behavior for ideal ALD growth mechanism was achieved at 450 ms for $TiCl_4$ and 300 ms for H_2O with a stable GPC value of 0.4 Å/cycle. The XPS measurements confirmed the presence of TiO_2 nanofilms on the AC substrates and found increased amounts of oxygen-containing functional groups while the lack of characteristic peaks in the XRD analysis suggests an amorphous crystal structure. Most importantly, the ALD-coated TiO_2 nanofilms were found to have exceptionally uniform surface coverage and conformity with the underlying

AC surface morphology as revealed by comprehensive studies of SEM, EDX, and TEM. In addition, the observed TiO_2 film thicknesses in high magnification TEM images are in excellent agreement with the measured values via ellipsometry on the co-loaded silicon substrates.

The effects of the TiO_2 nanofilms on the electrochemical performance of AC electrodes for SC applications were assessed quantitatively and qualitatively in extensive charge-discharge cycles and CV measurements. Based on the calculated C_s and ESR values, the optimal ALD process was found to be at 60 cycles with an estimated TiO_2 film thickness of 2.3 nm. The TiAC60 SC exhibited a remarkable 61% improvement in C_s compared to the bare AC. However, higher ESR values were observed on the TiO_2-coated AC SCs due to the increased oxygen-containing functional groups which acts as active sites for electrolyte decomposition and parasitic faradaic reactions. Nevertheless, these findings contribute new insights on the coating mechanisms of ALD technology on highly porous substrates to effectively decorate them with highly uniform and conformal TiO_2 nanofilms. This study provides the groundwork for a possible solution in producing high energy density SCs and unlocking their limited applications in the industry as next generation energy storage devices.

CRediT authorship contribution statement

Remuel Vitto: Electrode Fabrication, ALD, SEM, EDX, Electrochemical analysis, Writing – original draft, Visualization, Validation, Methodology, Investigation, Formal analysis, Data curation. **Hamed Pourkheirollah**: Electrode Fabrication, ALD, SEM, EDX, Electrochemical analysis, Writing – review & editing, Investigation, Formal analysis, Data curation. **Jari Keskinen**: Writing – review & editing, Investigation, Formal analysis, Methodology, Conceptualization. **Steffen Thrane Vindt**: Writing – review & editing, Investigation, Formal analysis. **Andrew Cook**: Writing – review & editing, Investigation, Formal analysis. **Līga Grīnberga**: Writing – review & editing, Investigation, Formal analysis. **Līga Ignatāne**: TEM, Writing – review & editing, Investigation, Formal analysis, Data curation. **Gints Kučinskis**: Writing – review & editing, Investigation, Formal analysis. **Amit Tewari**: Raman spectroscopy, XPS, Writing – review & editing, Investigation, Formal analysis, Data curation. **Donald Lupo**: Writing – review & editing, Methodology, Funding acquisition, Conceptualization. **Paul Berger**: ALD, Writing – review & editing, Methodology, Conceptualization. **Matti Mäntysalo**: Writing – review & editing, Supervision, Funding acquisition, Conceptualization.

Declaration of Competing Interest

The authors declare that they have no known competing financial interests or personal relationships that could have appeared to influence the work reported in this paper.

Acknowledgment

Funded by the European Union

GRAPHENE FLAGSHIP

This project, funded by the European Commission's Horizon Europe programme, is part of the Graphene Flagship initiative which works to advance technologies that rely on graphene and other 2D materials. Part of the research uses Research Council of Finland Research Infrastructure 'Printed Intelligence Infrastructure' (PII-FIRI, Grant Number 358618).

The x-ray diffraction measurements were performed at the Materials science and environmental engineering in Tampere University and the electron microscopy and elemental mapping analysis was performed at the Tampere Microscopy Center in Tampere University. We express our appreciation to Specialist Leo Hyvärinen from Tampere University for his assistance with the XRD analysis, and to Senior Scientist Mari Honkanen and Staff Scientist Kati Valtonen from Tampere University for their assistance with the FESEM-EDX characterizations.

Data Availability

Data and related metadata will be openly available in Zenodo at https://doi.org/10.5281/zenodo.15179824.

References

[1] Wong, S. I., Sunarso, J., Wong, B. T., Lin, H., Yu, A., & Jia, B. (2018). *Towards enhanced energy density of graphene-based supercapacitors: Current status, approaches, and Future Directions*. Journal of Power Sources, 396, 182–206. https://doi.org/10.1016/j.jpowsour.2018.06.004

[2] Khan, F. M. N., Rasul, M. G., Sayem, A. S. M., & Mandal, N. (2023). *Maximizing energy density of lithium-ion batteries for electric vehicles: A critical review*. Energy Reports, 9, 11–21. https://doi.org/10.1016/j.egyr.2023.08.069

[3] Wang, Q., Jiang, B., Li, B., & Yan, Y. (2016). *A critical review of thermal management models and solutions of lithium-ion batteries for the development of Pure Electric Vehicles*. Renewable and Sustainable Energy Reviews, 64, 106–128. https://doi.org/10.1016/j.rser.2016.05.033

[4] Zhang, J., Gu, M., & Chen, X. (2023). *Supercapacitors for renewable energy applications: A Review*. Micro and Nano Engineering, 21, 100229. https://doi.org/10.1016/j.mne.2023.100229

[5] Chen, X., Paul, R., & Dai, L. (2017). *Carbon-based supercapacitors for efficient energy storage*. National Science Review, 4(3), 453–489. https://doi.org/10.1093/nsr/nwx009

[6] Raghavendra, K. V., Vinoth, R., Zeb, K., Muralee Gopi, C. V. V., Sambasivam, S., Kummara, M. R., Obaidat, I. M., & Kim, H. J. (2020a). *An intuitive review of*

supercapacitors with recent progress and novel device applications. Journal of Energy Storage, 31, 101652. https://doi.org/10.1016/j.est.2020.101652

[7] Kanjana, N., Maiaugree, W., Lunnoo, T., Laokul, P., Inthira Chaiya, Ruammaitree, A., Wongjom, P., & Infahsaeng, Y. (2023). *One-step hydrothermal synthesis and electrocatalytic properties of MOS2/activated carbon composite derived from shallots*. Journal of Applied Electrochemistry, 53(12), 2311–2320. https://doi.org/10.1007/s10800-023-01921-z

[8] Gambou-Bosca, A., & Bélanger, D. (2015). *Chemical mapping and electrochemical performance of manganese dioxide/activated carbon based composite electrode for asymmetric electrochemical capacitor*. Journal of The Electrochemical Society, 162(5). https://doi.org/10.1149/2.0181505jes

[9] Cao, J.-P., He, S., Wu, Y., Zhao, X.-Y., Wei, X.-Y., & Takarada, T. (2017). *Synthesis of NIO/activated carbon composites and their application as electrode materials for capacitors*. International Journal of Electrochemical Science, 12(4), 2704–2718. https://doi.org/10.20964/2017.04.39

[10] Liu, Y.-H., Hsi, H.-C., Li, K.-C., & Hou, C.-H. (2016). *Electrodeposited manganese dioxide/activated carbon composite as a high-performance electrode material for Capacitive Deionization*. ACS Sustainable Chemistry & Engineering, 4(9), 4762–4770. https://doi.org/10.1021/acssuschemeng.6b00974

[11] Elmouwahidi, A., Bailón-García, E., Castelo-Quibén, J., Pérez-Cadenas, A. F., Maldonado-Hódar, F. J., & Carrasco-Marín, F. (2018). *Carbon–tio2 composites as high-performance supercapacitor electrodes: Synergistic effect between carbon and metal oxide phases*. Journal of Materials Chemistry A, 6(2), 633–644. https://doi.org/10.1039/c7ta08023a

[12] Lobiak, E. V., Bulusheva, L. G., Fedorovskaya, E. O., Shubin, Y. V., Plyusnin, P. E., Lonchambon, P., Senkovskiy, B. V., Ismagilov, Z. R., Flahaut, E., & Okotrub, A. V. (2017). *One-step chemical vapor deposition synthesis and supercapacitor performance of nitrogen-doped porous carbon–carbon nanotube hybrids*. Beilstein Journal of Nanotechnology, 8, 2669–2679. https://doi.org/10.3762/bjnano.8.267

[13] Weber, M., Boysen, N., Graniel, O., Sekkat, A., Dussarrat, C., Wiff, P., Devi, A., & Muñoz-Rojas, D. (2023). *Assessing the environmental impact of atomic layer deposition (ALD) processes and pathways to lower it*. ACS Materials Au, 3(4), 274–298. https://doi.org/10.1021/acsmaterialsau.3c00002

[14] Suntola, T. & Antson, J. (1977). *Method for producing compound thin films* (U.S. Patent No. 4058430 A).

[15] Ahmed, B., Xia, C., & Alshareef, H. N. (2016). *Electrode Surface Engineering by atomic layer deposition: A promising pathway toward Better Energy Storage*. Nano Today, 11(2), 250–271. https://doi.org/10.1016/j.nantod.2016.04.004

[16] Li, Z., Su, J., & Wang, X. (2021). *Atomic layer deposition in the development of supercapacitor and lithium-ion battery devices*. Carbon, 179, 299–326. https://doi.org/10.1016/j.carbon.2021.03.041

[17] Ansari, M. Z., Hussain, I., Mohapatra, D., Ansari, S. A., Rahighi, R., Nandi, D. K., Song, W., & Kim, S. (2023). *Atomic Layer Deposition—a versatile toolbox for designing/engineering electrodes for advanced supercapacitors*. Advanced Science, 11(1). https://doi.org/10.1002/advs.202303055

[18] Morozova, M., Kluson, P., Krysa, J., Vesely, M., Dzik, P., & Solcova, O. (2012). *Electrochemical properties of tio2 electrode prepared by various methods*. Procedia Engineering, 42, 573–580. https://doi.org/10.1016/j.proeng.2012.07.450

[19] Suzuki, T., Miura, N., Hojo, R., Yanagiba, Y., Suda, M., Hasegawa, T., Miyagawa, M., & Wang, R.-S. (2020). *Genotoxicity assessment of titanium dioxide nanoparticle accumulation of 90 days in the liver of GPT Delta transgenic mice*. Genes and Environment, 42(1). https://doi.org/10.1186/s41021-020-0146-3

[20] Kirkland, D., Aardema, M. J., Battersby, R. V., Beevers, C., Burnett, K., Burzlaff, A., Czich, A., Donner, E. M., Fowler, P., Johnston, H. J., Krug, H. F., Pfuhler, S., & Stankowski, L. F. (2022). *A weight of evidence review of the genotoxicity of titanium dioxide (tio2)*. Regulatory Toxicology and Pharmacology, 136, 105263. https://doi.org/10.1016/j.yrtph.2022.105263

[21] Wang, J., Polleux, J., Lim, J., & Dunn, B. (2007). *Pseudocapacitive contributions to electrochemical energy storage in tio2 (anatase) nanoparticles*. The Journal of Physical Chemistry C, 111(40), 14925–14931. https://doi.org/10.1021/jp074464w

[22] Brezesinski, T., Wang, J., Polleux, J., Dunn, B., & Tolbert, S. H. (2009). *Templated nanocrystal-based porous tio2 films for next-generation electrochemical capacitors*. Journal of the American Chemical Society, 131(5), 1802–1809. https://doi.org/10.1021/ja8057309

[23] Tan, D. Q., Song, G., Gandla, D., & Zhang, F. (2020). *Commonalities of atomic layer deposition of oxide coatings on activated carbons for 3.5 V electric double layer*

supercapacitors. Frontiers in Energy Research, 8. https://doi.org/10.3389/fenrg.2020.596062

[24] Bai, Y., Li, N., Yang, C., Wu, X., Yang, H., Chen, W., Li, H., Zhao, B., Wang, P.-F., & Han, X. (2021). *Realizing high-voltage and Ultralong-life supercapacitors by a Universal Interfacial Engineering Strategy*. Journal of Power Sources, 510, 230406. https://doi.org/10.1016/j.jpowsour.2021.230406

[25] Sun, X., Xie, M., Wang, G., Sun, H., Cavanagh, A. S., Travis, J. J., George, S. M., & Lian, J. (2012). *Atomic layer deposition of tio2on graphene for Supercapacitors*. Journal of The Electrochemical Society, 159(4). https://doi.org/10.1149/2.025204jes

[26] Sun, X., Xie, M., Travis, J. J., Wang, G., Sun, H., Lian, J., & George, S. M. (2013). *Pseudocapacitance of amorphous tio2 thin films anchored to graphene and carbon nanotubes using atomic layer deposition*. The Journal of Physical Chemistry C, 117(44), 22497–22508. https://doi.org/10.1021/jp4066955

[27] Fisher, R. A., Watt, M. R., Konjeti, R., & Ready, W. J. (2014). *Atomic layer deposition of titanium oxide for pseudocapacitive functionalization of vertically-aligned carbon nanotube supercapacitor electrodes*. ECS Journal of Solid State Science and Technology, 4(2). https://doi.org/10.1149/2.0141502jss

[28] Ritala, M., Leskelä, M., Nykänen, E., Soininen, P., & Niinistö, L. (1993). *Growth of titanium dioxide thin films by Atomic Layer Epitaxy*. Thin Solid Films, 225(1–2), 288–295. https://doi.org/10.1016/0040-6090(93)90172-l

[29] Standard, B. B. (2006). *Fixed electric double layer capacitors for use in electronic equipment*. Part I: Generic specification. BS EN, 62391-1.

[30] Profijt, H. B., Potts, S. E., van de Sanden, M. C., & Kessels, W. M. (2011). *Plasma-assisted atomic layer deposition: Basics, opportunities, and challenges*. Journal of Vacuum Science & Technology A: Vacuum, Surfaces, and Films, 29(5). https://doi.org/10.1116/1.3609974

[31] Pourkheirollah, H., Keskinen, J., Mäntysalo, M., & Lupo, D. (2022). *An improved exponential model for charge and discharge behavior of printed supercapacitor modules under varying load conditions*. Journal of Power Sources, 535, 231475. https://doi.org/10.1016/j.jpowsour.2022.231475

[32] Illers, K.-H. (1971). *Geordnete Strukturen in „amorphem“ polyäthylenterephthalat*. Colloid and Polymer Science, 245(1), 393–398. https://doi.org/10.1007/bf01501003

[33] Diaham, S. (2021). *Polyimide in electronics: Applications and Processability Overview*. Polyimide for Electronic and Electrical Engineering Applications. https://doi.org/10.5772/intechopen.92629

[34] Hofmann, K., Hegde, A. D., Liu-Theato, X., Gordon, R., Smith, A., & Willenbacher, N. (2024). *Effect of mechanical properties on processing behavior and electrochemical performance of aqueous processed graphite anodes for lithium-ion batteries*. Journal of Power Sources, 593, 233996. https://doi.org/10.1016/j.jpowsour.2023.233996

[35] TA Instruments - Materials Science Solutions. Thermal analysis and rheology of anodes. *TGA thermal stability and compositional amount of anode materials*. Available at https://www.tainstruments.com/applications/battery-material-testing/anode/

[36] Tewari, A., Gandla, S., Bohm, S., McNeill, C. R., & Gupta, D. (2019). *Remarkable wettability of highly dispersive RGO ink on multiple substrates independent of deposition techniques*. FlatChem, 16, 100110. https://doi.org/10.1016/j.flatc.2019.100110

[37] Groppo, E., Bonino, F., Cesano, F., Damin, A., & Manzoli, M. (2018). Chapter 4. *Raman, IR and INS Characterization of functionalized carbon materials*. Catalysis Series, 103–137. https://doi.org/10.1039/9781788013116-00103

[38] Turner, J., Aspinall, H. C., Rushworth, S., & Black, K. (2019). *A hybrid nanoparticle/alkoxide ink for inkjet printing of Tio2: A templating effect to form anatase at 200 °C*. RSC Advances, 9(67), 39143–39146. https://doi.org/10.1039/c9ra06119c

[39] Morais, A., Alves, J. P., Lima, F. A., Lira-Cantu, M., & Nogueira, A. F. (2015). *Enhanced photovoltaic performance of inverted hybrid bulk-heterojunction solar cells using tio 2 /reduced graphene oxide films as electron transport layers*. Journal of Photonics for Energy, 5(1), 057408. https://doi.org/10.1117/1.jpe.5.057408

[40] Tewari, A., Böhm, S., Gandla, S., McNeill, C. R., & Gupta, D. (2017). *Graphene-mwnts composite coatings with enhanced electrical conductivity*. FlatChem, 4, 33–41. https://doi.org/10.1016/j.flatc.2017.06.011

[41] Mevada, C., Tissari, J., Parihar, V. S., Tewari, A., Keskinen, J., & Mäntysalo, M. (2024). *Bio-inspired 3D-printed supercapacitors for Sustainable Energy Storage*. Journal of Power Sources, 624, 235529. https://doi.org/10.1016/j.jpowsour.2024.235529

[42] Zhang, L., Tu, L., Liang, Y., Chen, Q., Li, Z., Li, C., Wang, Z., & Li, W. (2018). *Coconut-based activated carbon fibers for efficient adsorption of various organic dyes*. RSC Advances, 8(74), 42280–42291. https://doi.org/10.1039/c8ra08990f

[43] Mahdi, N., Kumar, P., Goswami, A., Perdicakis, B., Shankar, K., & Sadrzadeh, M. (2019). *Robust polymer nanocomposite membranes incorporating discrete tio2*

nanotubes for water treatment. Nanomaterials, 9(9), 1186. https://doi.org/10.3390/nano9091186

[44] Fic, K., Platek, A., Piwek, J., & Frackowiak, E. (2018). *Sustainable materials for electrochemical capacitors*. Materials Today, 21(4), 437–454. https://doi.org/10.1016/j.mattod.2018.03.005

[45] Wang, B., Jin, P., Yue, Y., Ji, S., Li, Y., & Luo, H. (2015). *Synthesis of nacl single crystals with defined morphologies as templates for fabricating hollow nano/micro-structures*. RSC Advances, 5(7), 5072–5076. https://doi.org/10.1039/c4ra15385e

[46] Qiu, C., Jiang, L., Gao, Y., & Sheng, L. (2023). *Effects of oxygen-containing functional groups on carbon materials in supercapacitors: A Review*. Materials &; Design, 230, 111952. https://doi.org/10.1016/j.matdes.2023.111952

[47] Eleri, O. E., Azuatalam, K. U., Minde, M. W., Trindade, A. M., Muthuswamy, N., Lou, F., & Yu, Z. (2020). Towards high-energy-density supercapacitors via less-defects activated carbon from Sawdust. Electrochimica Acta, 362, 137152. https://doi.org/10.1016/j.electacta.2020.137152

[48] Sen, R., Das, S., Nath, A., Maharana, P., Kar, P., Verpoort, F., Liang, P., & Roy, S. (2022). *Electrocatalytic Water Oxidation: An overview with an example of translation from lab to market*. Frontiers in Chemistry, 10. https://doi.org/10.3389/fchem.2022.861604